

Prohibitin 1 is essential to preserve mitochondria and myelin integrity in Schwann cells.

Gustavo Della-Flora Nunes

Hunter James Kelly Research Institute, School of Medicine and Biomedical Sciences, University at Buffalo <https://orcid.org/0000-0001-9323-3556>

Emma Wilson

Hunter James Kelly Research Institute, School of Medicine and Biomedical Sciences, University at Buffalo <https://orcid.org/0000-0002-8069-0173>

Leandro Marziali

Hunter James Kelly Research Institute, School of Medicine and Biomedical Sciences, University at Buffalo

Edward Hurley

State University of New York at Buffalo

Nicholas Silvestri

Hunter James Kelly Research Institute, School of Medicine and Biomedical Sciences, University at Buffalo

Bin He

Houston Methodist Research Institute

Bert O'Malley

Baylor College of Medicine <https://orcid.org/0000-0003-3332-1399>

Bogdan Beirowski

University at Buffalo <https://orcid.org/0000-0002-1241-1777>

Yannick Poitelon

Albany Medical College

Lawrence Wrabetz

Hunter James Kelly Research Institute, School of Medicine and Biomedical Sciences, University at Buffalo

M. Laura Feltri (✉ mlfeltri@buffalo.edu)

Hunter James Kelly Research Institute, School of Medicine and Biomedical Sciences, University at Buffalo <https://orcid.org/0000-0002-2276-9182>

Article

Keywords: PHB1, neuropathy, myelin maintenance, demyelination, integrated stress response

Posted Date: August 28th, 2020

DOI: <https://doi.org/10.21203/rs.3.rs-54990/v1>

License:  This work is licensed under a Creative Commons Attribution 4.0 International License.

[Read Full License](#)

Version of Record: A version of this preprint was published at Nature Communications on June 2nd, 2021. See the published version at <https://doi.org/10.1038/s41467-021-23552-8>.

Abstract

Myelin is required for nervous system function. In the peripheral nervous system, Schwann cells (SCs) form myelin and trophically support the axons they ensheath. We previously showed that the mitochondrial protein prohibitin 2 (PHB2) can localize to the axon-SC interface and is required for developmental myelination. Whether the homologous protein PHB1 has a similar role, and whether prohibitins also play important roles in SC mitochondria is unknown. Here we show that deletion of Phb1 in SCs only minimally perturbs development, but later triggers a severe demyelinating peripheral neuropathy. Moreover, mitochondria are heavily affected by ablation of Phb1 and demyelination occurs preferentially in cells with apparent mitochondrial loss. Furthermore, in response to mitochondrial damage, SCs trigger the integrated stress response (ISR), but, contrary to what was previously suggested, the ISR is not detrimental and may be beneficial in this context. These results identify a new role for PHB1 in myelin integrity and advance our understanding of how SCs respond to mitochondrial damage.

1. Introduction

In the peripheral nervous system (PNS), Schwann cells (SCs) surround axons with myelin, a multi-layered lipid-rich membrane essential for rapid and efficient propagation of nerve signals. The myelination process is metabolically-demanding, requiring massive biosynthesis of lipids and proteins in a short period of time. In rodents, it is estimated that the total membrane area of a SC expands up to 6,500 times during myelination¹. Furthermore, the PNS has an exquisite organization, with many long axons either completely myelinated or fully surrounded by non-myelinated SCs, which severely limits direct contact between the axons and the extracellular environment. Therefore, SCs are also believed to provide axons with metabolic and trophic support, a function that seems to be independent from myelination². As a consequence, SC metabolism likely needs to be tightly regulated to allow both myelination and axonal support.

Mitochondria, which are pivotal organelles in cellular metabolism, are quickly emerging as important regulators of myelin formation and maintenance in SCs. Peripheral neuropathy is a common manifestation of genetic mitochondrial disorders, affecting about 30% of all patients³. Moreover, in those cases where the neuropathy is demyelinating, morphological alterations frequently concentrate in mitochondria of SCs rather than axons, suggesting a link between mitochondrial dysfunction in SCs and demyelination⁴. Recently, two different studies showed that deletion of mitochondrial genes in SCs results in peripheral neuropathy in mice^{5,6}. However, the mechanisms by which dysfunctional SC mitochondria lead to demyelination remain incompletely understood.

We recently identified prohibitin 2 (PHB2) as an essential protein for developmental myelination in mice⁷. Moreover, we found evidence that PHB2 can localize to the axon-SC interface and is important in the early contact between these two cell types⁷. Although prohibitins have been reported in diverse subcellular localizations, they are most well known for their role in mitochondria, where they carry out many of their

functions⁸. In the mitochondria, PHB2 associates with the homologous protein PHB1, forming a large oligomeric ring-like structure in the inner mitochondrial membrane⁹. This structure is thought to act as a platform that aids in the regulation of several aspects of mitochondrial biogenesis, dynamics and metabolism^{8,10}. Thus, we set out to investigate the role of PHB1 in Schwann cells *in vivo*.

Here we show that, contrary to deletion of *Phb2*, deletion of *Phb1* in SCs causes only a minimal developmental phenotype, but triggers a severe demyelinating peripheral neuropathy after myelination is completed. A careful characterization of potential functions of PHB1 revealed that mitochondria were heavily affected, and that mitochondrial damage was progressive and accumulated in single cells. Interestingly, we found a sudden loss of mitochondrial content in discrete cells, which was associated with demyelination. We also confirmed that the cellular response to mitochondrial damage in SCs involves the integrated stress response (ISR), but, contrary to what has been previously suggested¹¹, we demonstrate that the ISR is not detrimental, and may even be beneficial in the context of demyelination induced by mitochondrial injury in SCs. These results advance our understanding of how SCs respond to mitochondrial damage, solidify the importance of SC mitochondria to maintain nerve homeostasis and reveal that, unexpectedly, PHB1 and PHB2 may have some independent functions.

2. Results

2.1. Schwann cell specific knockout of *Phb1*

Given the involvement of PHB2 in developmental myelination⁷, we sought to investigate the role PHB1 plays in Schwann cells (SCs) *in vivo*. To this end, we crossed mice bearing a floxed *Phb1* gene¹² with mice expressing *Cre* recombinase under the control of the *Mpz* promoter¹³. This allowed us to generate mice in which *Phb1* was deleted specifically in SCs (*Phb1^{fl/fl}; Mpz-Cre* – referred to as Phb1-SCKO throughout) (Fig. 1A). Recombination in sciatic nerves of Phb1-SCKO animals was confirmed by PCR (Fig. 1B) and resulted in significant reduction of *Phb1* mRNA (Fig. 1C) and protein (**Supplementary Fig. 1A and 1B**).

2.2. Deletion of prohibitin 1 in SCs triggers a severe peripheral neuropathy

We then examined the morphology of sciatic nerves of Phb1-SCKO mice at different days of post-natal development: P10, P20, P40, P60, P90 and P120. Ablation of *Phb1* does not impair radial sorting like deletion of *Phb2*⁷, but leads to delayed myelination with most SCs still at the pro-myelinating stage in P10 animals (**Supplementary Fig. 1C and 1D**). However, by P20, Phb1-SCKO mice have an equivalent number of myelinated axons when compared to controls (Fig. 1D **and E**), even if they are slightly hypomyelinated (**Supplementary Fig. 1E**). Strikingly, this almost complete recovery from the developmental delay is then followed by a rapid and profound demyelination, which leads to a 60%

reduction in the number of myelinated fibers of Phb1-SCKO mice between P20 and P60 (Fig. 1D, E). Morphologically, demyelination is suggested by the presence of several large axons devoid of myelin and by SCs containing myelin debris in cytosolic compartments (Fig. 1D-F). Concomitant to the demyelination, we also identified signs of axonal degeneration, such as axonal shrinkage and local accumulation of vesicles and organelles, indicative of transport defects (Fig. 1F). In addition, Phb1-SCKO crossed to a Thy-1 YFP axonal reporter line present with evident axonal swellings and axon fragmentation in tibial nerves at P20 and P40, respectively (Fig. 1G). This peripheral neuropathy also leads to clear functional impairments in Phb1-SCKO mice. Mutant mice show reduced nerve conduction velocity at P20 and P40 and decreased compound muscle action potential (CMAP) amplitude at P40 (Fig. 1H), in addition to reduced motor performance in the rotarod test at P20 (**Supplementary Fig. 1F**). In line with the typical manifestation of peripheral neuropathy in mice, Phb1-SCKO animals show clenching of hind limbs towards the body when suspended by the tail (**Supplementary Fig. 1G**). Moreover, these animals show clear gait impairments that progress to hind limb paresis or paralysis (**Supplementary Video 1**).

2.3. The Peripheral neuropathy caused by Phb1 deletion affects different types of nerve fibers

Previous studies have suggested that different aspects of SC metabolism are important to maintain homeostasis of distinct types of nerve fibers in the PNS. For example, deletion of the mitochondrial transcription factor *Tfam* in SCs results in a sensory-motor demyelinating neuropathy⁶. On the other hand, ablation of the metabolic regulator *Lkb1* in SCs causes myelination delay later followed by widespread degeneration of Remak bundles, with no demyelination¹⁴. Therefore, we first asked if specific types of fibers were more affected in Phb1-SCKO mice. The size distribution of myelinated axons in sciatic nerves, which contain both motor and sensory fibers, was similar between Phb1-SCKO and controls (**Supplementary Figs. 2A and 2B**), suggesting that demyelination equally affects fibers of all calibers. As previously reported, the distribution of demyelinated axons was smaller than to the distribution of myelinated axons in Phb1-SCKO animals (**Supplementary Figs. 2C and 2D**), in line with previous findings that demyelination results in reduction of axon caliber due to decreased neurofilament phosphorylation¹⁵, which might be a consequence of loss of myelin and trophic support from SCs.

We also directly investigated if the peripheral neuropathy was prominent in both the motor and sensory compartments by comparing the primarily sensory saphenous nerve and the motor branch of the femoral nerve (**Supplementary Fig. 3A**). Phb1-SCKO animals show a reduction of myelinated fibers and presence of demyelinated fibers in both the femoral motor and the saphenous nerve (**Supplementary Figs. 3B and 3C, respectively**). Therefore, Phb1 deletion from SCs causes a sensory-motor peripheral neuropathy.

Last, we examined the effect of Phb1 ablation on Remak SCs, which surround non-myelinated small caliber axons. At P20, Phb1-SCKO mice had a typical density of Remak bundles, which also displayed normal organization with well-ensheathed axons in the correct number and size (**Supplementary Fig. 4**). However, at P40 several Remak SCs of Phb1-SCKO mice seemed to have retracted their processes,

resulting in many axons directly abutting each other (**Supplementary Fig. 4**). This phenomenon was somewhat lessened at P90; but, at this age, Remak bundles of *Phb1*-SCKO mice were fragmented, which resulted in reduced number of axons per Remak bundle and increased density of Remak bundles (**Supplementary Fig. 4B**). In addition, at P90, Remak bundles of *Phb1*-SCKO mice tended to contain abnormally large axons. In combination, these results may reflect an attempt of the Remak SCs to respond to the ongoing demyelination by: 1) transdifferentiating to a SC type that promote nerve repair; 2) ensheathing some small demyelinated axons. Alternatively, Remak SCs of *Phb1*-SCKO mice may be simply dysfunctional, causing fragmentation of the Remak bundle and axonal swelling.

2.4 Macrophage infiltration, ERK activation and Schwann cell death are unlikely to be causes of the neuropathy in *Phb1*-SCKO mice

For all the subsequent analyses, we focused on three time points: P20, P40 and P90, which represent beginning, mid and late stages of the peripheral neuropathy, respectively. It is a reasonable assumption that alterations that are already present at P20 are more likely to be causal for the phenotype, while alterations that appear at the P40 or P90 time points are most likely secondary phenomena that originate as a consequence of the pathology.

Given that prohibitins are required for activation of the Raf-MEK-ERK pathway by Ras¹⁶ and that this is an important pathway for myelination¹⁷ and demyelination¹⁸, we first asked whether *Phb1* deletion in SCs affected ERK1/2 expression or phosphorylation. (Surprisingly, we only found minor changes in p-ERK1/2 and total ERK1/2 at P40 (**Supplementary Fig. 5A and 5B**).

A common feature of peripheral neuropathies is the presence of macrophages, which infiltrate the nerves to phagocytize myelin and cellular debris. In some occasions, macrophages can be involved with the initiation of peripheral neuropathies and cause demyelination¹⁹. Thus, we asked if macrophages were present in the nerves of *Phb1*-SCKO mice before demyelination. An elevated number of macrophages is detectable in P40 and P90 *Phb1*-SCKO animals in comparison to controls (**Supplementary Fig. 5C**), but there are no differences at P20 (**Supplementary Fig. 5**). The timing of macrophage infiltration (P40) coincides with the elevation of ERK1/2 phosphorylation (**Supplementary Fig. 5B**) and of *Mcp1* upregulation (**Supplementary Fig. 5E**), a chemokine previously shown to be secreted by SCs and fibroblasts downstream of ERK signaling to promote macrophage recruitment²⁰. Therefore, it is possible that all these events are linked, but they are more likely a consequence, rather than a cause of demyelination.

Prohibitins are often necessary to maintain cell survival and support cell proliferation²¹. In fact, knockdown of either *Phb1* or *Phb2* in isolated primary rat SCs leads to cell death⁷. Thus, we investigated whether SC death or proliferation were altered *in vivo* in nerves of *Phb1*-SCKO mice. At P20, there were no differences between groups in TUNEL assay and staining for phosphorylated Histone 3 (p-H3; a mitotic

marker) (**Supplementary Fig. 6A and 6B**). However, nerves of Phb1-SCKO animals showed a slight increase in both TUNEL + and p-H3 + cells at P40 and P90 (**Supplementary Fig. 6A and 6B**). We further confirmed that TUNEL + and proliferating cells were SCs by co-staining with SOX10 (**Supplementary Fig. 6C and 6D**). Nonetheless, changes in cell survival and proliferation were tardy and modest and thus unlikely to be sufficient and timely to cause the phenotype. In addition, the balance between cell death and cell division seems to be maintained, since nerves of Phb1-SCKO contain normal quantities of SCs at P20 and P40 (**Supplementary Fig. 6E**).

2.5. Ablation of prohibitin 1 causes mitochondrial damage accumulation

Prohibitins are mainly localized in the mitochondria, where they are essential for its structure and function. Prohibitins are important for many mitochondrial functions, including fusion, cristae morphogenesis²², mtDNA maintenance²³, stabilization of respiratory complexes^{24,25} and prevention of ROS production²⁶. Thus, we expected that mitochondria would be primarily and severely affected in Phb1-SCKO animals. Analyses by electron microscopy revealed aberrant mitochondrial morphology (Fig. 2A), with SCs of Phb1-SCKO mice showing increased mitochondrial perimeter at all evaluated time points (Fig. 2B-D). Mitochondrial swelling is typical of dysfunctional mitochondria and is associated with several pathological conditions²⁷.

To investigate SC mitochondria in more detail, we crossed Phb1-SCKO animals to PhAM mice²⁸, a flox-STOP mitochondrial fluorescent reporter. The *Mpz-Cre* mediated recombination of PhAM exclusively in SCs allows for a selective evaluation of fluorescent SC mitochondria without confounding results from the large number of mitochondria present in axons. We analyzed confocal images of sciatic nerve teased fibers using an automated routine for ImageJ, which allowed quantification of mitochondrial volume in different compartments in the SC. At P20, larger size mitochondria are overrepresented around the endoplasmic reticulum (ER) and in Cajal bands of Phb1-SCKO animals compared to controls, while mitochondria in juxtaparanodes show a shift toward smaller sizes (Fig. 2E, quantified in **Supplementary Fig. 7**). We also identified a trend toward increased mitochondrial numbers in Cajal bands of Phb1-SCKO mice (**Supplementary Fig. 7B**). At P40, aberrant SC mitochondrial patterning in Phb1-SCKO mice persists, with altered size distribution of mitochondria in the vicinity of Cajal bands, the nodes/paranodes and by this age present also in Remak SCs, suggesting mitochondrial fragmentation (**Supplementary Fig. 9**). Strikingly, at P40, many myelinating SCs of Phb1-SCKO mice displayed almost complete absence of PhAM signal in portions of the SC away from the cell body (Fig. 2F, arrows). This was a phenomenon affecting about 20% of all myelinating fibers of Phb1-SCKO animals (Fig. 2G), while it was not detected in P20 Phb1-SCKO mice (data not shown). In addition, other mitochondrial markers, such as HSPD1 and TOM20 were also severely reduced in SCs in which PhAM was undetectable (**Supplementary Fig. 8**). This likely reflects the amplification of the early mitochondrial dysfunction seen at P20 and consequent elimination of damaged mitochondria. In line with this hypothesis, there is a progressive depletion of

mtDNA from sciatic nerves of Phb1-SCKO animals (Fig. 3A). This mosaic pattern of mitochondrial loss could be explained by the progressive accumulation and amplification of mitochondrial derangements in specific SCs.

To investigate if altered mitochondrial dynamics could be contributing to the mitochondrial alterations in Phb1-SCKO mice, we performed live imaging of SCs isolated from Phb1^{wt/wt}; P0-Cre; PhAM (Control) and Phb1^{fl/fl}; P0-Cre; PhAM (Phb1-SCKO) animals. We exposed a focal region of the SCs to the 405 nm confocal laser to promote photoconversion of PhAM from green to red and then monitored cells for 30 min. In control SCs, photoconverted (red) mitochondria dispersed quickly and no peak in the red signal is evident at the end of the experiment (Fig. 3B). On the other hand, red SC mitochondria are still present as a group after 30 min in Phb1-SCKO mice (Fig. 3B **and Supplementary Videos 2 and 3**). This indicates that deletion of *Phb1* in SCs leads to impaired mitochondrial dynamics and/or transport. Impaired mitochondrial dynamics could be a consequence of dysfunctional Opa1, a dynamin-related GTPase involved in fusion of the inner mitochondrial membrane. Deletion of prohibitins has been previously reported to trigger proteolytic cleavage of Opa1, impairing its function²². In agreement with this hypothesis, Western blots from sciatic nerve lysates show increased proteolytic processing of Opa1 in Phb1-SCKO mice (Fig. 3C).

Next, we asked whether these mitochondrial changes affected mitochondrial physiology and function. We evaluated mitochondrial membrane potential using TMRM in SCs isolated from control and Phb1-SCKO animals. Ablation of Phb1 results in significant reduction in TMRM fluorescence suggesting that mitochondria of Phb1-SCKO mice are depolarized (Figs. 3D and 3E). Since the mitochondrial membrane potential relates to the cell's capacity to make ATP through oxidative phosphorylation, we also evaluated mitochondrial respiration using the Seahorse Extracellular Flux Analyzer. Since SCs of Phb1-SCKO mice have impaired survival *in vitro* and a relatively large number of cells were required for this analysis, we instead acutely knocked down *Phb1* in primary rat SCs using shRNA. Our analyses revealed normal basal respiration in *Phb1*-knockdown SCs, but a significant decrease in the spare respiratory capacity compared to cells treated with sh-Control (Figs. 3F-3I). This result indicates that SCs lacking PHB1 may be unable to appropriately respond to changes in metabolic demand.

A common consequence of inefficient respiration in a situation of stress is the production of reactive oxygen species by mitochondria. However, we did not detect any difference in lipoperoxidation or protein oxidation between nerves of Phb1-SCKO mice and controls (**Supplementary Fig. 10**), suggesting that, at least at the time points examined, oxidative stress may not be present.

Prohibitin 2 has recently been described as a mitophagy receptor at the inner mitochondrial membrane²⁹. Although it is not clear if Prohibitin 1 also participate in mitophagy, we postulated that PHB1-ablated Schwann cells may accumulate damaged mitochondria because they may be unable to perform mitophagy. We thus analyzed the capacity of PHB1-ablated Schwann cells to carry out mitophagy. For

these analyses, we made use of a retrovirus system to deliver mt-mKeima, a mitochondrially-targeted pH-sensitive fluorescent protein³⁰. When in the mitochondria (which has a neutral pH), the mt-mKeima excitation peak is at 440 nm. However, when mitochondria are targeted to degradation in the lysosomes (therefore reducing the pH), the excitation peak of mt-mKeima shifts to 586 nm. Thus, a ratio of the mt-mKeima fluorescence at ~ 586 nm over the fluorescence at ~ 440 nm can be used as a proxy for the degree of mitochondrial degradation in the lysosomes. Using this method, we found that silencing of *Phb1* by shRNA does not change the ability of SCs to perform mitophagy (**Supplementary Fig. 11**).

We next tested if there is an association between mitochondrial damage and demyelination in *Phb1*-SCKO mice. To this end, we analyzed teased fibers from *Phb1*^{wt/wt}; P0-Cre; PhAM (Control) and *Phb1*^{fl/fl}; P0-Cre; PhAM (*Phb1*-SCKO) animals. In *Phb1*-SCKO animals, fibers with undetectable PhAM were overrepresented among fibers containing myelin ovoids, suggesting an association between mitochondrial damage and demyelination (**Supplementary Fig. 12**).

Taken together, our results indicate that mitochondria in SCs of *Phb1*-SCKO mice are severely impaired starting at P20. In addition, we show evidence that mitochondrial dysfunction and demyelination are linked and that the mitochondrial damage is accumulating, possibly because *Phb1*-SCKO mice have abnormal mitochondrial dynamics.

2.6. Deletion of *Phb1* activates a mitochondrial stress response

Although mitochondria have their own DNA, they still depend on genomic DNA to synthesize most of their proteins (only 13 out of more than 1200 mitochondrial proteins are coded by mtDNA)³¹. Thus, in order to keep homeostasis, there is a need for bidirectional mitonuclear communication³². In a similar fashion, when mitochondria are under stress, cells respond with a coordinated attempt to mitigate potential damage. In mammals, this normally involves activation of the integrated stress response (ISR), a general stress pathway working to reduce overall protein synthesis and favor the expression of stress-response genes³³. A previous report by Viader et al. showed that deletion of the mitochondrial transcription factor *Tfam* in SCs results in activation of the ISR, which they postulated to be a maladaptive mechanism¹¹. Thus, we asked whether *Phb1* deletion in SCs triggers the ISR by assessing the levels of phosphorylated eIF2 α , the hallmark of ISR. Indeed, we found that nerves of *Phb1*-SCKO mice showed early (P20) and continually elevated levels of phosphorylated eIF2 α in comparison to littermate controls (Fig. 4A).

We then sought to investigate the downstream events in this mitochondrial stress response. Classically, mitochondrial dysfunction induces the mitochondrial unfolded protein response (UPR^{mt}), which results in upregulation of a set of genes including mitochondrial chaperones (such as *Hspd1* and *Hspe1*, also known as *Hsp60* and *Hsp10*, respectively) and proteases (such as *Clpp*). Thus, we probed *Phb1*-SCKO animals for the activation of UPR^{mt}. Surprisingly, we did not detect elevation of any UPR^{mt} effector at protein or RNA level (Figs. 4B-4D). A recent publication implicated ATF4 in the mammalian mitochondrial stress response and characterized the molecular signature of this pathway³⁴. Therefore, we assessed this

pathway in nerves of Phb1-SCKO mice. Even though *Atf4* expression itself is not altered by deletion of *Phb1* in SCs, four out of the five analyzed transcripts regulated by ATF4 are upregulated in nerves of Phb1-SCKO mice (Fig. 4E): *Asns* (asparagine synthetase); *Chac1* (cation transport regulator-like protein 1); *Pck2* (phosphoenolpyruvate carboxykinase 2) and *Ddit3* (DNA damage-inducible transcript 3; also known as *Chop*). Importantly, phosphorylation of eIF2 α in this context does not seem to be triggered by activation of PERK kinase in the ER, since its phosphorylation is not increased (**Supplementary Figs. 13A and 13B**). However, Phb1-SCKO mice do show elevated levels of the HSPA chaperone (also known as Bip) (**Supplementary Fig. 13C**), and upregulated alternative splicing of *Xbp1* (**Supplementary Fig. 13D**), two markers commonly associated with the unfolded protein response in the ER (UPR^{ER}). This suggests that mitochondrial dysfunction caused by Phb1-SCKO indirectly leads to ER stress.

The ER is an organelle involved in lipid synthesis, while mitochondria take part in beta-oxidation, the process of breakdown of fatty acids. Therefore, it is possible that the balance of lipid metabolism is altered in Phb1-SCKO mice. If lipid oxidation occurs disproportionately to lipid synthesis, myelin maintenance could be affected due to depletion of important myelin lipids. This mechanism has been previously proposed to underlie the peripheral neuropathy caused by deletion of *Tfam* in SCs¹¹. Therefore, we evaluated the expression and phosphorylation of Acetyl-CoA carboxylase (ACC). The ACC enzyme is responsible for production of malonyl-CoA, the substrate for biosynthesis of fatty acids and an inhibitor of beta-oxidation. ACC activity is inhibited by phosphorylation at Ser79 by AMPK or at Ser1200 by PKA. Nerves of Phb1-SCKO mice showed increased phosphorylated ACC at P20 (Fig. 5A-D). Moreover, the expression of many genes involved with lipid synthesis is severely reduced (Fig. 5E and 15F) at both P20 and P40, suggesting that reduction of lipid biosynthesis might be a common finding in neuropathies in which SC mitochondria are damaged.

In summary, ablation of *Phb1* in SCs leads not only to a mitochondrial stress response involving the ISR, but also to a broader cellular response, affecting the ER and causing reduced expression of enzymes involved in lipid biosynthesis.

2.7. The mitochondrial stress response is beneficial to Phb1-SCKO mice

Given the dramatic implications of the ISR for cells, such as a widespread inhibition of translation, we aimed to test if continuous activation of the ISR was maladaptive in the context of mitochondrial dysfunction in SCs, as suggested by Viader et al.¹¹. To evaluate the role of ISR in Phb1-SCKO mice, we treated animals daily from P20 to P40 with 2.5 mg/kg of ISRIB (for ISR inhibitor). Unphosphorylated eIF2 transfers the methionylated initiator tRNA (Met-tRNA) to the ribosome in a guanosine 5'-triphosphate-dependent manner to start translation³⁵. Phosphorylation of the alpha subunit of eIF2 leads to competitive inhibition of eIF2B, the guanosine-exchange factor (GEF) for eIF2, halting translation³⁶. IRSIB

is a small molecule known to enhance the GEF activity of eIF2B, thereby alleviating the translation block^{37,38} (Fig. 6A).

As expected, ISRIB treatment did not change p-eIF2 α levels (Fig. 6B), but significantly reduced the upregulation of ATF4 target genes in Phb1-SCKO mice (Fig. 6C). In tibial nerves, we identified a small reduction in myelin thickness (g-ratio = the ratio between axon and fiber diameters) in larger caliber axons due to Phb1 deletion in SCs, which was accompanied by a reduction in overall axon caliber. However, there was no significant effect of ISRIB on these parameters (**Supplementary Fig. 14**). Surprisingly, additional morphological analysis of tibial nerves of Phb1-SCKO mice treated with ISRIB, revealed an exacerbation of the demyelination (Fig. 6D). Supporting this conclusion, quantifications showed an increased number of demyelinated axons and of myelin degradation in Phb1-SCKO mice upon ISRIB treatment (Fig. 6E). In line with our morphological findings, Phb1-SCKO animals treated with ISRIB showed a trend toward reduced performance in the rotarod test as compared to Phb1-SCKO mice treated with vehicle (p-values Phb1-SCKO + ISRIB vs Phb1-SCKO + Veh: Day 2 = 0.0936, Day 3 = 0.0979, Day 4 = 0.0723) (Fig. 6F).

Taken together, our results suggest that activation of the ISR not only is not detrimental, but may even be a protective mechanism against demyelination triggered by deletion of Phb1.

3. Discussion

In this study, we investigated the role of PHB1 in SCs using conditional knockout mice. We found that ablation of Phb1 from SCs leads to a mild developmental delay in myelination followed by a severe and quickly progressing demyelinating peripheral neuropathy. This contrasts with the severe and persistent myelination arrest that we observed as a consequence of deletion of *Phb2* in SCs⁷. Given that PHB1 and PHB2 are thought to always act as partners, and that their protein levels are believed to be mutually regulated^{22,39}, it will be interesting to investigate if this difference reflects a peculiar biology of prohibitins in SCs. In particular, it is possible that PHB1 and PHB2 play diverse roles during myelination and myelin maintenance in the PNS. We hypothesize that, during development, PHB2 has extra-mitochondrial activities necessary for proper radial sorting (the process by which axons are selected to be myelinated), while both PHB1 and PHB2 may be required in mitochondria for long-term myelin maintenance. It is also possible that our results are pointing to previously unappreciated differences in the roles of PHB1 and PHB2, which may also be conserved in other cell types.

Prohibitins can perform a wide range of biological functions and have been described in different cellular compartments²¹. However, both PHB1 and PHB2 are generally concentrated in the mitochondria of all investigated cell types⁸. Accordingly, we report that mitochondria are heavily affected in SCs lacking *Phb1*, with PHB1 being critical for regulation of mitochondrial morphology, mitochondrial dynamics, mitochondrial membrane potential, mitochondrial respiration and maintenance of mtDNA. These

morphological and functional perturbations to mitochondria accumulate as the demyelinating neuropathy progresses in *Phb1*-SCKO mice. Unexpectedly, we identified that the pattern of mitochondrial damage progressed to apparent loss of mitochondria in discrete cells, which correlated with demyelination. Therefore, dysfunction in SC mitochondria seems to be mechanistically linked to demyelination (see schematics in Fig. 6G). This is important because mitochondria with aberrant morphology are often found in SCs from patients affected by neuropathies of several etiologies, including mitochondrial disorders⁴⁰, inherited neuropathies⁴¹ and diabetes⁴². Therefore, SC mitochondria are important players in peripheral neuropathies.

To our knowledge, there are only a few reports that explored the impact of loss of function of mitochondrial proteins in SCs. Conditional deletion of the respiratory chain component *Cox10* results in severe dysmyelination in the PNS, with many axons remaining unmyelinated despite being correctly sorted⁵. This could suggest that mitochondrial energy production is necessary for proper myelination. However, SCs can tolerate a significant reduction in ATP levels without any noticeable effect in myelin formation or maintenance, as described by our group when *Pdha1* (which codes for an essential subunit of the pyruvate dehydrogenase complex, a mitochondrial enzyme) was deleted in SCs⁴³. Ablation of the mitochondrial network regulator *Gdap1* in SCs leads to an age-related hypomyelinating peripheral neuropathy, recapitulating aspects of the Charcot–Marie–Tooth disease seen in patients with mutated *Gdap1*⁴⁴. Deletion of mitochondrial *m*-AAA protease in SCs in adult animals results in the presence of a few demyelinated axons long-term⁴⁵. In addition, Remak SCs lacking *m*-AAA seem to retract their processes from between the axons⁴⁵, an observation similar to our findings in *Phb1*-SCKO mice at P40. This is interesting since prohibitins are believed to regulate the proteolytic activity of the *m*-AAA protease⁴⁶ and, thus, effects of *Phb1* deletion may be partially mediated through the *m*-AAA protease. Finally, SC-specific ablation of the mitochondrial transcription factor *Tfam* triggers a progressive demyelinating peripheral neuropathy⁶, a phenotype similar to the one observed in *Phb1*-SCKO mice. Combined, the results from *Gdap1*, *m*-AAA and *Tfam* conditional knockout mice suggest that SC mitochondrial function is critical to maintain PNS myelin long-term. Viader et al. proposed that a deregulation of lipid metabolism caused by a maladaptive integrated stress response (ISR) could underlie the phenotype seen in *Tfam*-SCKO mice¹¹. We also observed a significant downregulation of enzymes involved with lipid biosynthesis in *Phb1*-SCKO and, thus, this could be a common perturbation caused by disruption of mitochondrial function in SCs. However, it is still unknown if this alteration to lipid metabolism is solely responsible for the phenotype of *Tfam*-SCKO mice, and it is possible that there are other mechanisms connecting mitochondrial function to preservation of peripheral nerves.

A particularly interesting hypothesis is that demyelination happens inadvertently as SCs try to cope with the mitochondrial damage. For this reason, we also investigated how SCs respond to mitochondrial dysfunction. In the absence of *Phb1*, SCs do not initiate the classical UPR^{mt}, first characterized in invertebrates, but instead activate a mitochondrial stress response involving the ISR and ATF4. Indeed, this was recently shown to be the canonical response of mammalian cells to mitochondrial damage^{47,48}. Viader et al., proposed that a maladaptive ISR leading to altered lipid metabolism underlies the

neuropathy of Tfam-SCKO mice¹¹. This hypothesis is particularly attractive since the ISR is known to be causal for nerve pathology in the context of ER stress⁴⁹. With this in mind, we investigated the role of ISR in Phb1-SCKO mice. Surprisingly, inhibition of the ISR in Phb1-SCKO mice using ISRIB seems to exacerbate the demyelinating neuropathy, indicating that the ISR may be a beneficial response in SCs with perturbed mitochondrial function. An exciting prediction from these findings is that the ISR elicited by mitochondrial dysfunction may have different downstream effects compared to the ISR triggered upon ER stress, something that we would like to explore in the future. It is also possible that, although central to the mitochondrial stress response, the ISR is not the only pathway activated upon mitochondrial damage. Investigation of these responses in SCs can provide further insight on how mitochondrial dysfunction leads to demyelination.

In conclusion, this study reveals that Phb1-SCKO mice show a phenotype distinct from the previously described Phb2-SCKO animals⁷, an unexpected finding that may also be relevant for the study of the biology of prohibitins in other cell types. The rapid demyelinating peripheral neuropathy observed in Phb1-SCKO mice seems to be significantly more severe than that of previous conditional knockout mice for mitochondrial genes. This may be due to the extensive roles that PHB1 plays in mitochondrial biology. One important aspect of mitochondrial function modulated by PHB1 is mitochondrial dynamics. Interestingly, we show that Phb1-SCKO mice seem to have impaired mitochondrial dynamics, accumulation of mitochondrial damage and preferential demyelination of cells with apparent mitochondrial loss. Further studies should investigate the cellular alterations in SCs that link mitochondrial damage to demyelination; but, according to our data, it is unlikely that this mechanism involves the ISR. In fact, it seems that the mitochondrially-induced ISR is beneficial in the context of demyelination in the PNS. Our study adds to the growing body of research demonstrating the crucial role for SC mitochondria to maintain nerve homeostasis. Given the results of this and other reports, perturbations of SC mitochondria are sufficient to elicit severe nerve damage and, therefore, should be viewed as possible mechanisms underlying peripheral neuropathies.

4. Materials And Methods

4.1. Animal models

All animal experiments were approved by the Institutional Animal Care and Use Committee (IACUC) of the Roswell Park Cancer Institute and the regulatory authorities at the University at Buffalo. Animals were housed separated by gender in groups of at most five per cage and kept in a 12 h light/dark cycle. Mpz-Cre and Phb1 floxed animals were previously described^{12,13}. Mice were also crossed to Thy1-YFP^{50,51} and PhAM²⁸ reporter lines. Animals were kept in a C57BL/6 and 129 mixed genetic background and analyses were only performed from littermates. Animals carrying one or two floxed *Phb1* alleles but no Cre were used as controls, unless otherwise specified. No animals were excluded from this study. Genotyping was performed from genomic DNA as previously described for Mpz-Cre¹³ and Phb1 floxed animals¹². Verification of recombination of floxed Phb1 was also previously reported¹². For Thy1-YFP,

genotyping primers used were F: 5' acagacacacaccagga 3' and R: 5' cggtggtgcagatgaactt 3' and PCR conditions were 94 °C for 4 min, (94 °C for 20 sec, 65 °C for 15 sec and 68 °C for 10 sec) in the first 10 cycles, (94 °C for 15 sec, 60 °C for 15 sec and 72 °C for 10 sec) for 28 cycles and 78 °C for 5 min. The Thy1-YFP transgene resulted in a 400 bp band. For the PhAM PCR, primers used were F: 5' ccaaagtcgctctgagttgttatc 3' WT R: 5' gagcgggagaaatggatatg 3' and PhAM R: 5' caatgggcggggggtcgtt 3'. PCR conditions were 95 °C for 3 min, (95 °C for 30 sec, 56 °C for 40 sec and 72 °C for 1 min) for 30 cycles and 72 °C for 7 min. The PhAM transgene resulted in a ~ 350 bp band, while the WT yielded a band at ~ 650 bp. ISRIB (Cayman chemicals # 16258) was prepared as described previously⁵² and administered intraperitoneally at 2.5 mg/kg from P20 to P40.

4.2. Morphological assessments

Mice were euthanized at the indicated ages and sciatic, tibial, femoral motor and saphenous nerves were dissected and processed as previously reported⁴³. For g-ratio analyses, four images per nerve were acquired using the 100X objective and axon and fiber diameters were calculated using a semi-automated protocol in the Leica QWin software (Leica Microsystem). For morphological quantifications, images were acquired with the 100X objective and stitched using the PTGui software v.10 (New House Internet Services BV) to reconstruct a complete image of the nerve. Morphological parameters were then evaluated in the full nerve. Electron micrographs at 2,900X were used for all the quantifications described below. For the mitochondrial perimeter, at least 100 mitochondria per animal were evaluated. For quantifications of axonal size, random images were selected and about 100 myelinated axons and 50 demyelinated axons were measured per animal. For analysis of Remak bundles, about 30 random fields were assessed. Unless stated otherwise, quantifications were performed using ImageJ Fiji v1.52p^{53,54}.

4.3. Behavioral and electrophysiological analyses

Rotarod was performed as described elsewhere⁵⁵. Briefly, animals were tested in two daily sessions (minimum 6 h rest in between) for two consecutive days in an accelerating rotarod (4 to 40 rpm in 5 min). Each session included three trials, and the average time on the rod per session was reported.

Electrophysiological analyses were performed as described⁴³, and distal amplitude and average nerve conduction velocity are reported.

4.4. Cell culture and *Phb1* knockdown

Primary rat SCs were isolated from P3 rat sciatic nerves as reported previously⁵⁶. Cells were not passaged more than four times and were maintained in media containing high glucose DMEM (4.5 g/L glucose) supplemented with 10% fetal bovine serum (FBS), 2 mM L-glutamine, 100 U/mL penicillin, 100 µg/mL streptomycin, 2 ng/ml Nrg1 (human NRG1-β1 extracellular domain, R&D Systems), and 2 µM forskolin. For the knockdown of *Phb1*, shRNA constructs (#1 = TRCN088454 and #2 = TRCN087986; Thermo Fisher Scientific) were packaged in lentiviral vectors as previously described⁷. A scramble shRNA construct was used as control. Primary rat SCs were transduced with the lentivirus and kept in culture for 72 h after transduction. Mouse primary SCs were prepared using a protocol modified from⁵⁷: Adult

sciatic nerves from 2–3 animals per genotype were dissected, stripped from epineurium and other contaminant tissues and kept in culture for 7 days to allow formation of repair SCs. Media formulation was identical to media used for rat SCs, except for use of 10 ng/ml Nrg1 (human NRG1- β 1 extracellular domain, R&D Systems). After 7 days, cells were dissociated enzymatically using a mixture of 2.5 mg/mL of dispase II (Sigma-Aldrich) and 130U/mL of type I collagenase (Worthington Biochemical Corporation) for 3 h at 37 °C, mechanically dissociated using fire-polished glass pipettes and seeded on one 35 mm dish coated with laminin (Sigma-Aldrich). Mouse SCs were maintained for up to a week in high glucose DMEM (4.5 g/L glucose) supplemented with 2 mM L-glutamine, 100 U/mL penicillin, 100 μ g/mL streptomycin, 2 ng/ml Nrg1 (human NRG1- β 1 extracellular domain, R&D Systems) and N2 supplement (Thermo Fisher Scientific). Cells were passaged once onto the appropriate plates for each experiment.

4.5. Seahorse analysis

Cellular bioenergetics analysis was performed using a Seahorse XFp instrument and the mitochondrial stress test (Agilent), following the manufacturer's instructions. Primary rat SCs were plated in Poly-L-Lysine coated wells of the XFp plate in a number that resulted in a confluent layer of cells by the time of the analysis: 6,000 cells in each well to be transduced with control shRNA and 12,000 cells in each well to be transduced with the *Phb1* shRNAs. The difference in seeding density aimed to equilibrate the cell number at the time of the experiment, since *Phb1* knockdown caused cell death. Transduction with shRNAs was performed 24 h after cell seeding and the Seahorse analysis was carried out 72 h after transduction. For the Seahorse experiment, 1.5 μ M oligomycin was used to inhibit mitochondrial ATP synthesis, 2 μ M FCCP was used to stimulate maximal mitochondrial respiration and 0.5 μ M Rotenone and 0.5 μ M Antimycin A were used to completely block mitochondrial respiration. During the assay, cells were kept in non-buffered XF DMEM medium pH 7.4 supplemented with 1 mM pyruvate, 2 mM glutamine, and 10 mM glucose. At the end of the assay, cell nuclei were stained with Hoechst 33342 (Thermo Fisher Scientific) and a Biotek Cytation 5 plate reader was utilized to obtain an automated cell count. Basal and maximal respiration were calculated using the Agilent Seahorse XF Cell Mito Stress Test Report Generator and were normalized by cell number.

4.6. Immunofluorescence and quantifications

For analysis of Thy-YFP, tibial nerves were dissected, fixed in 4% PFA for 30 min and tissue was whole-mounted for visualization. The general immunofluorescence protocol involved permeabilization of the tissue using acetone or methanol, blocking for 1 h at room temperature, incubation with primary antibodies overnight at 4 °C, incubation with secondary antibodies for 1 h at room temperature, counterstain with DAPI and mounting of slides with Vectashield (Vector Laboratories). Blocking buffer 1 was used for sections and contained 20% FBS, 1% bovine serum albumin and 0.1% Triton X-100 in 1X PBS. Blocking buffer 2 was used for teased fibers and contained 5% fish skin gelatin and 0.1% Triton X-100 in 1X PBS. Below we describe particularities of each experiment. For analyses involving the PhAM transgene, sciatic nerves were dissected, fixed in 4% PFA for 30 min, washed with PBS and teased in slides coated with (3-Aminopropyl) triethoxysilane (TESPA; Sigma). For co-staining, the following primary antibodies were used: rabbit anti-KDEL 1:500 (Thermo Fisher Scientific #PA1-013), rabbit anti-Kv1.1 1:200

(Alomone #APC-009), rabbit anti-p75^{NTR} 1:1500 (Cell signaling #8238), rabbit anti-S100 β 1:200 (Daki #ZO311), chicken anti-Neurofascin 1:1000 (R&D Systems #AF3235), rabbit anti-TOM20 1:500 (Proteintech #11802-1-AP), rabbit anti-HSPD1 1:500 (Proteintech # 15282-1-AP), chicken anti-P0 1:300 (Aves #PZO0308) and Mouse anti-MBP (Smi99) 1:500 (Biolegend #808401). Staining for TOM20 required no permeabilization. Images for all the above experiments were acquired using a confocal microscope Leica SP5II. For quantification of mitochondrial size and location, 1024 \times 1024 pixel z-stacks were acquired with a 100X objective and 1.5X zoom, using the system-optimized z-step size to allow oversampling of the z plane. Quantifications were performed automatically using the 3D ImageJ Suite⁵⁸ on ImageJ Fiji v1.52p. The automated routine included: filtering of the image stacks using a Median 3D Fast Filter with x, y and z radius of 2 px; identification of the cellular location based on the staining in the red channel using 3D Hysteresis Thresholding algorithm (high = 30 low = 15); identification of the mitochondria in the green channel using 3D Iterative Thresholding (min_vol_pix = 20 max_vol_pix = 700 min_threshold = 3 min_contrast = 0 criteria_method = MSER threshold_method = STEP segment_results = All value_method = 10); and measurements of mitochondrial volume, sphericity and distance of each mitochondrion to the cellular location using the 3D RoiManager. Mitochondria were considered in the vicinity of a given cellular location if they were no more than 2 μ m distant from that location. Secondary antibodies used in this study were Alexa 488 Donkey anti-rabbit IgG 1/1000 (Jackson ImmunoResearch #711-545-152), Cy3 Donkey anti-chicken IgY 1/500 (Jackson ImmunoResearch #703-165-155), Cy3 Donkey anti-mouse IgG 1/500 (Jackson ImmunoResearch #715-165-150) and Rhodamine (TRITC) anti-rabbit IgG 1/500 (Jackson ImmunoResearch #711-025-152).

4.7. Live imaging

In all live imaging experiments, cells were maintained in media prepared with Fluorobrite DMEM (Thermo Fischer Scientific A1896701) and with N2 supplement (Thermo Fisher Scientific) instead of regular DMEM and FBS. For analyses of mitochondrial dynamics and mitophagy, cells were maintained at 37 °C and 5% CO₂ using a live imaging stage coupled to the Leica SP5II confocal microscope. For assessment of mitochondrial dynamics, primary mouse Schwann cells were isolated from Control and Phb1-SCKO mouse expressing mito-dendra2 (PhAM reporter) and plated in Lab-Tek chamber slides coated with laminin. In each experiment, we pooled cells from 2–3 animals for each genotype. Data reported represent results from two independent experiments. For each cell, a circular ROI of the same size was established about a third of the way in one of its processes. To promote photoconversion of mito-dendra2, this region was stimulated with the 405 nm laser at 20% power for 128 iterations. Cells were then monitored for 30 min using the 488 nm and the 561 nm laser lines to stimulate mito-dendra2 in the unconverted and photoconverted state, respectively. Images were obtained using a 40X objective and 3X zoom. Post-acquisition, intensity on red channel was analyzed using the Dynamic ROI Profiler on ImageJ Fiji v1.52p by establishing a line with its center passing through the photoconverted area. For analysis of mitochondrial membrane potential, primary mouse SCs were isolated from control and Phb1-SCKO mice (pool of 4 animals each). 10,000 SCs were seeded in a glass-bottom 96-well plate coated with laminin. Cells were incubated for 30 min with 50 nM Mitotracker green (Thermo Fischer Scientific # M7514) and 20 nM TMRM (Thermo Fischer Scientific #I34361) and immediately imaged using a Biotek Cytation 5

plate reader. Hepes 25 nM was added to maintain the pH and plates were kept at 37 °C during incubation and acquisition. 2 μ M FCCP was used as a positive control to cause mitochondrial depolarization. Four images per well were acquired from six wells per genotype. Cells with morphology not compatible with SCs were excluded from analysis. Quantifications were performed using auto-thresholding in ImageJ Fiji v1.52p and the ratio between the TMRM and Mitotracker green signals is reported.

4.8. Western blot

Sciatic nerves were dissected, epineurium and other contaminant tissues were removed and samples were snap frozen in liquid nitrogen and stored at -80 °C until processing (except for analysis of p-PERK, when protein extraction and SDS-PAGE were carried out right after dissection). Nerves were pulverized and resuspended in lysis buffer [50 mM Tris pH 7.4, 150 mM NaCl, 1% IGEPAL CA-630, 1 mM EDTA, 1 mM EGTA, 0.1% SDS, 0.5% sodium deoxycholate, 1 mM sodium orthovanadate, 1 mM sodium fluoride, protease inhibitor cocktail (Sigma P8340), phosphatase inhibitor cocktail 2 (Sigma P5726) and phosphatase inhibitor cocktail 3 (Sigma P0044)]. After lysis, samples were sonicated in a water sonicator with three cycles of 20 s at 70% power and then centrifuged at 16,000 rpm for 30 min at 4 °C.

Supernatant was collected and protein concentration was determined by BCA protein assay (Thermo Scientific) according to the manufacturer's instructions. Equal amounts of protein per sample were diluted 3:1 in 4X Laemmli (250 mM Tris-HCl pH 6.8, 8% SDS, 5% β -Mercaptoethanol, 40% Glycerol, 0.04% Bromophenol blue) and denatured for 5 min at 100 °C. Samples were then loaded on an SDS-polyacrylamide gel and electroblotted onto a PVDF membrane. Blots were then blocked with 5% BSA in TBS-T (1X TBS + 0.1% Tween-20) and incubated overnight with the appropriate primary antibody: Phb1 1:500 (Abcam #ab28172), Opa1 1:500 (Thermo Fischer Scientific # 612606), Erk1/2 1:500 (Cell signaling #9102), p-ERK1/2 1:500 (Cell signaling #9101), β -tubulin 1:5000 (Novus Biologicals #NB600-936), TOM20 1:500 (BD Biosciences #612278), GAPDH 1:5000 (Sigma #G9545), eIF2 α 1:500 (Cell signaling #5324), p-eIF2 α 1:500 (Cell signaling #3398), Clpp 1:500 (Proteintech #15698-1-AP), Hspd1 1:500 (Proteintech #15282-1-AP), PERK 1:500 (Cell signaling #3192), p-PERK 1:500 (Cell signaling #3179), Bip 1:500 (Novus Biologicals #NB300-520), ACC 1:500 (Cell signaling #3662), p-ACC 1:500 (Cell signaling #3661). Membranes were then rinsed in 1X TBS-T and incubated for 1 h with secondary antibodies. Blots were either imaged directly with Odyssey CLx infrared imaging system (Li-Cor) or developed using ECL Select (GE Healthcare) and imaged using a ChemiDoc XRS system. Quantifications were carried out in the Image lab 6.0 software (Biorad) for blots imaged with the ChemiDoc XRS or in the Image Studio Lite 5.2 (Odyssey) for blots imaged with the Odyssey CLx. GAPDH or β -tubulin were used as the loading control. All uncropped blots are presented in **Supplementary Fig. 15**.

4.9. RNA extraction and qRT-PCR analyses

RNA was isolated and reverse-transcribed as published⁵⁹. qRT-PCR for lipid metabolism and for quantification of mtDNA used the SYBR green method and primers as reported previously¹¹. For quantification of spliced Xbp1 (sXbp1), we used the Taqman assay-on-Demand Mm03464496_m1 (Applied Biosystems) and normalized data to results using probe Mm99999915_g1 to detect the housekeeping gene *Gapdh*. All the other assays were carried out using the Universal Probe library from

Roche Diagnostic. For the analysis, Faststart Universal Probe Master (Rox) (Sigma #4913949001) was mixed with the following combination of primers (reported 5' to 3') and probes: *Phb1* (F: gggctcctgccttctatcacc, R: tcaattctccagcatcgaatc, Probe #77), *Ddit3* (F: accaccacacctgaaagca, R: gacctcctgcagatcctcat, Probe #11), *Atf4* (F: tataaagggcgggttaggg, R: acttaaaccggcagacagca, Probe #70), *Clpp* (F: gagctttcccgctcatcc, R: ggccacactgtcgtcaatc, Probe #22), *Asns* (F: ggccacactgtcgtcaatc, R: aggaaggaagggctccact, Probe #22), *Chac1* (F: gtatcacctgcccattgttcc, R: aagagctacttcgctccttc, Probe #56), *Pck2* (F: ggcagagcacatgctgatt, R: gccacgtagcgtttttc, Probe #9), *Psph* (F: agcctgtcctcctgctgat, R: gtaccactggcggtgtcct, Probe #62), *Hspd1* (F: cagtggaaatccggagagg, R: aggttagactgtttcttaagttcagc, Probe #89), *Hspe1* (F: ggcccagattcagagtcc, R: ctgtcaaagagcggagaagaac, Probe #62), *Mcp1* (F: catccacgtgttggtca, R: gatcatctgtcgtgtaagt, Probe #56), *Actb* (β -actin) (F: aaggccaaccgtgaaaagat, R: gtggtacgaccagaggcatac, Probe #77). Data were normalized to the housekeeping gene β -actin. All assays were performed using a Bio-Rad CFX96/384 real-time PCR machine using the following cycle: 50 °C for 2 min, 95 °C for 10 min and (95 °C for 10 sec and 60 °C for 30 sec) for 40 cycles. Data were analyzed using the threshold cycle (Ct) and $2(-\Delta\Delta Ct)$ method, and average expression of control animals was normalized to 1.

4.10. Statistical analyses

Experiments (with the exception of assigning animals to ISRIB or Veh groups) were not randomized, but data collection and analysis were performed blind to the conditions of the experiments and genotype of the mice where applicable. No data were excluded from the analyses. No power analysis was performed, but our sample sizes are similar to those generally used in the field. The statistical test used in each analysis is reported in the legend of every figure. Data are presented as mean \pm s.e.m. Values of $P < 0.05$ were considered to represent a significant difference, while $P < 0.1$ was considered to represent a trend. Data were analyzed using GraphPad Prism 6.01.

5. Data Availability

The data supporting the findings of this study are available within the article and its supplementary information files. All original data are available from the corresponding author upon reasonable request.

Declarations

Data availability

The data supporting the findings of this study are available within the article and its supplementary information files. All original data are available from the corresponding author upon reasonable request.

Competing interests

The authors declare no competing interests.

Acknowledgements

We thank J. Catlin and S. S. Rasam for assistance performing the UPR^{mt} WB and TBARS experiments, respectively. This work was funded by grant NIH-NINDS-R01NS100464 (to M.L.F.). Generation of the Phb1-floxed animals was originally supported by National Institutes of Health Grants HD08818 and HD07857 to B.W.O.

Author contributions

G.D.N., Y.P., and M.L.F. designed research and interpreted data; G.D.N. Carried out the majority of the experiments; Y.P. performed the proliferation and TUNEL analyses in 20-day-old mice; L.N.M. and E.H. prepared and processed the tissue for morphological analyses; N.S. performed the electrophysiology analysis; B.H. and B.W.O. provided the Phb1 floxed mice; B.B. provided technical assistance for the Seahorse analysis; G.D.N. and M.L.F. wrote the manuscript; E.R.W., Y.P., L.W., B.B., B.W.O. and B.H. analyzed the data and critically reviewed the manuscript.

References

1. Chrast, R., Saher, G., Nave, K. A. & Verheijen, M. H. Lipid metabolism in myelinating glial cells: lessons from human inherited disorders and mouse models. *J Lipid Res* 52, 419–434, doi:10.1194/jlr.R009761 (2011).
2. Nave, K. A. Myelination and the trophic support of long axons. *Nat Rev Neurosci* 11, 275–283, doi:10.1038/nrn2797 (2010).
3. Pareyson, D., Piscoquito, G., Moroni, I., Salsano, E. & Zeviani, M. Peripheral neuropathy in mitochondrial disorders. *Lancet Neurol* 12, 1011–1024, doi:10.1016/s1474-4422(13)70158-3 (2013).
4. Ino, D. & Iino, M. Schwann cell mitochondria as key regulators in the development and maintenance of peripheral nerve axons. *Cell Mol Life Sci* 74, 827–835, doi:10.1007/s00018-016-2364-1 (2017).
5. Funfschilling, U. *et al.* Glycolytic oligodendrocytes maintain myelin and long-term axonal integrity. *Nature* 485, 517–521, doi:10.1038/nature11007 (2012).
6. Viader, A. *et al.* Schwann cell mitochondrial metabolism supports long-term axonal survival and peripheral nerve function. *J Neurosci* 31, 10128–10140, doi:10.1523/jneurosci.0884-11.2011 (2011).
7. Poitelon, Y. *et al.* Spatial mapping of juxtacrine axo-glial interactions identifies novel molecules in peripheral myelination. *Nat Commun* 6, 8303, doi:10.1038/ncomms9303 (2015).
8. Artal-Sanz, M. & Tavernarakis, N. Prohibitin and mitochondrial biology. *Trends Endocrinol Metab* 20, 394–401, doi:10.1016/j.tem.2009.04.004 (2009).
9. Tatsuta, T., Model, K. & Langer, T. Formation of membrane-bound ring complexes by prohibitins in mitochondria. *Mol Biol Cell* 16, 248–259, doi:10.1091/mbc.e04-09-0807 (2005).

10. Merkwirth, C. & Langer, T. Prohibitin function within mitochondria: essential roles for cell proliferation and cristae morphogenesis. *Biochim Biophys Acta* 1793, 27–32, doi:10.1016/j.bbamcr.2008.05.013 (2009).
11. Viader, A. *et al.* Aberrant Schwann cell lipid metabolism linked to mitochondrial deficits leads to axon degeneration and neuropathy. *Neuron* 77, 886–898, doi:10.1016/j.neuron.2013.01.012 (2013).
12. He, B. *et al.* Estrogen-regulated prohibitin is required for mouse uterine development and adult function. *Endocrinology* 152, 1047–1056, doi:10.1210/en.2010-0732 (2011).
13. Feltri, M. L. *et al.* P0-Cre transgenic mice for inactivation of adhesion molecules in Schwann cells. *Ann N Y Acad Sci* 883, 116–123 (1999).
14. Beirowski, B. *et al.* Metabolic regulator LKB1 is crucial for Schwann cell-mediated axon maintenance. *Nat Neurosci* 17, 1351–1361, doi:10.1038/nn.3809 (2014).
15. de Waegh, S. M., Lee, V. M. & Brady, S. T. Local modulation of neurofilament phosphorylation, axonal caliber, and slow axonal transport by myelinating Schwann cells. *Cell* 68, 451–463 (1992).
16. Rajalingam, K. *et al.* Prohibitin is required for Ras-induced Raf-MEK-ERK activation and epithelial cell migration. *Nat Cell Biol* 7, 837–843, doi:10.1038/ncb1283 (2005).
17. Ishii, A., Furusho, M. & Bansal, R. Sustained activation of ERK1/2 MAPK in oligodendrocytes and schwann cells enhances myelin growth and stimulates oligodendrocyte progenitor expansion. *J Neurosci* 33, 175–186, doi:10.1523/jneurosci.4403-12.2013 (2013).
18. Napoli, I. *et al.* A central role for the ERK-signaling pathway in controlling Schwann cell plasticity and peripheral nerve regeneration in vivo. *Neuron* 73, 729–742, doi:10.1016/j.neuron.2011.11.031 (2012).
19. Allard, D. E. *et al.* Schwann cell-derived periostin promotes autoimmune peripheral polyneuropathy via macrophage recruitment. *J Clin Invest* 128, 4727–4741, doi:10.1172/jci99308 (2018).
20. Fischer, S., Weishaupt, A., Troppmair, J. & Martini, R. Increase of MCP-1 (CCL2) in myelin mutant Schwann cells is mediated by MEK-ERK signaling pathway. *Glia* 56, 836–843, doi:10.1002/glia.20657 (2008).
21. Thuaud, F., Ribeiro, N., Nebigil, C. G. & Desaubry, L. Prohibitin ligands in cell death and survival: mode of action and therapeutic potential. *Chem Biol* 20, 316–331, doi:10.1016/j.chembiol.2013.02.006 (2013).
22. Merkwirth, C. *et al.* Prohibitins control cell proliferation and apoptosis by regulating OPA1-dependent cristae morphogenesis in mitochondria. *Genes Dev* 22, 476–488, doi:10.1101/gad.460708 (2008).
23. Kasashima, K., Sumitani, M., Satoh, M. & Endo, H. Human prohibitin 1 maintains the organization and stability of the mitochondrial nucleoids. *Exp Cell Res* 314, 988–996, doi:10.1016/j.yexcr.2008.01.005 (2008).
24. Jian, C. *et al.* Deficiency of PHB complex impairs respiratory supercomplex formation and activates mitochondrial flashes. *J Cell Sci* 130, 2620–2630, doi:10.1242/jcs.198523 (2017).
25. Strub, G. M. *et al.* Sphingosine-1-phosphate produced by sphingosine kinase 2 in mitochondria interacts with prohibitin 2 to regulate complex IV assembly and respiration. *Faseb j* 25, 600–612,

- doi:10.1096/fj.10-167502 (2011).
26. Zhou, P. *et al.* Prohibitin reduces mitochondrial free radical production and protects brain cells from different injury modalities. *J Neurosci* 32, 583–592, doi:10.1523/jneurosci.2849-11.2012 (2012).
 27. Javadov, S., Chapa-Dubocq, X. & Makarov, V. Different approaches to modeling analysis of mitochondrial swelling. *Mitochondrion* 38, 58–70, doi:10.1016/j.mito.2017.08.004 (2018).
 28. Pham, A. H., McCaffery, J. M. & Chan, D. C. Mouse lines with photo-activatable mitochondria to study mitochondrial dynamics. *Genesis* 50, 833–843, doi:10.1002/dvg.22050 (2012).
 29. Wei, Y., Chiang, W. C., Sumpter, R., Jr., Mishra, P. & Levine, B. Prohibitin 2 Is an Inner Mitochondrial Membrane Mitophagy Receptor. *Cell* 168, 224–238.e210, doi:10.1016/j.cell.2016.11.042 (2017).
 30. Lazarou, M. *et al.* The ubiquitin kinase PINK1 recruits autophagy receptors to induce mitophagy. *Nature* 524, 309–314, doi:10.1038/nature14893 (2015).
 31. Baker, M. J., Tatsuta, T. & Langer, T. Quality control of mitochondrial proteostasis. *Cold Spring Harb Perspect Biol* 3, doi:10.1101/cshperspect.a007559 (2011).
 32. Quiros, P. M., Mottis, A. & Auwerx, J. Mitonuclear communication in homeostasis and stress. *Nat Rev Mol Cell Biol* 17, 213–226, doi:10.1038/nrm.2016.23 (2016).
 33. Pakos-Zebrucka, K. *et al.* The integrated stress response. *EMBO Rep* 17, 1374–1395, doi:10.15252/embr.201642195 (2016).
 34. Quiros, P. M. *et al.* Multi-omics analysis identifies ATF4 as a key regulator of the mitochondrial stress response in mammals. *J Cell Biol* 216, 2027–2045, doi:10.1083/jcb.201702058 (2017).
 35. Jackson, R. J., Hellen, C. U. & Pestova, T. V. The mechanism of eukaryotic translation initiation and principles of its regulation. *Nat Rev Mol Cell Biol* 11, 113–127, doi:10.1038/nrm2838 (2010).
 36. Hinnebusch, A. G. & Lorsch, J. R. The mechanism of eukaryotic translation initiation: new insights and challenges. *Cold Spring Harb Perspect Biol* 4, doi:10.1101/cshperspect.a011544 (2012).
 37. Kashiwagi, K. *et al.* Structural basis for eIF2B inhibition in integrated stress response. *Science* 364, 495–499, doi:10.1126/science.aaw4104 (2019).
 38. Kenner, L. R. *et al.* eIF2B-catalyzed nucleotide exchange and phosphoregulation by the integrated stress response. *Science* 364, 491–495, doi:10.1126/science.aaw2922 (2019).
 39. Coates, P. J. *et al.* Mammalian prohibitin proteins respond to mitochondrial stress and decrease during cellular senescence. *Exp Cell Res* 265, 262–273, doi:10.1006/excr.2001.5166 (2001).
 40. Schröder, J. M. Neuropathy Associated with Mitochondrial Disorders. *Brain Pathology* 3, 177–190, doi:10.1111/j.1750-3639.1993.tb00742.x (1993).
 41. Schroder, J. M. & Sommer, C. Mitochondrial abnormalities in human sural nerves: fine structural evaluation of cases with mitochondrial myopathy, hereditary and non-hereditary neuropathies, and review of the literature. *Acta Neuropathol* 82, 471–482, doi:10.1007/bf00293381 (1991).
 42. Kalichman, M. W., Powell, H. C. & Mizisin, A. P. Reactive, degenerative, and proliferative Schwann cell responses in experimental galactose and human diabetic neuropathy. *Acta Neuropathol* 95, 47–56, doi:10.1007/s004010050764 (1998).

43. Della-Flora Nunes, G. *et al.* Acetyl-CoA production from pyruvate is not necessary for preservation of myelin. *Glia* 65, 1626–1639, doi:10.1002/glia.23184 (2017).
44. A, N. *et al.* The Gdap1 Knockout Mouse Mechanistically Links Redox Control to Charcot-Marie-Tooth Disease. *Brain* 137, 668–682, doi:10.1093/brain/awt371 (2014).
45. S, W. *et al.* The Mitochondrial m-AAA Protease Prevents Demyelination and Hair Greying. *PLoS Genetics* 12, doi:10.1371/journal.pgen.1006463 (2016).
46. Steglich, G., Neupert, W. & Langer, T. Prohibitins regulate membrane protein degradation by the m-AAA protease in mitochondria. *Mol Cell Biol* 19, 3435–3442 (1999).
47. Fessler, E. *et al.* A pathway coordinated by DELE1 relays mitochondrial stress to the cytosol. *Nature* 579, 433–437, doi:10.1038/s41586-020-2076-4 (2020).
48. Guo, X. *et al.* Mitochondrial stress is relayed to the cytosol by an OMA1-DELE1-HRI pathway. *Nature* 579, 427–432, doi:10.1038/s41586-020-2078-2 (2020).
49. Pennuto, M. *et al.* Ablation of the UPR-mediator CHOP Restores Motor Function and Reduces Demyelination in Charcot-Marie-Tooth 1B Mice. *Neuron* 57, doi:10.1016/j.neuron.2007.12.021 (2008).
50. Feng, G. *et al.* Imaging neuronal subsets in transgenic mice expressing multiple spectral variants of GFP. *Neuron* 28, 41–51, doi:10.1016/s0896-6273(00)00084-2 (2000).
51. Ey, B., Kobsar, I., Blazyca, H., Kroner, A. & Martini, R. Visualization of degenerating axons in a dysmyelinating mouse mutant with axonal loss. *Mol Cell Neurosci* 35, 153–160, doi:10.1016/j.mcn.2007.02.014 (2007).
52. Chou, A. *et al.* Inhibition of the integrated stress response reverses cognitive deficits after traumatic brain injury. *Proc Natl Acad Sci U S A* 114, E6420–e6426, doi:10.1073/pnas.1707661114 (2017).
53. Rueden, C. T. *et al.* ImageJ2: ImageJ for the next generation of scientific image data. *BMC Bioinformatics* 18, 529, doi:10.1186/s12859-017-1934-z (2017).
54. Schindelin, J. *et al.* Fiji: an open-source platform for biological-image analysis. *Nat Methods* 9, 676–682, doi:10.1038/nmeth.2019 (2012).
55. Poitelon, Y. *et al.* Behavioral and molecular exploration of the AR-CMT2A mouse model Lmna (R298C/R298C). *Neuromolecular Med* 14, 40–52, doi:10.1007/s12017-012-8168-z (2012).
56. Brockes, J. P., Fields, K. L. & Raff, M. C. Studies on cultured rat Schwann cells. I. Establishment of purified populations from cultures of peripheral nerve. *Brain Res* 165, 105–118, doi:10.1016/0006-8993(79)90048-9 (1979).
57. Manent, J., Oguievetskaia, K., Bayer, J., Ratner, N. & Giovannini, M. Magnetic cell sorting for enriching Schwann cells from adult mouse peripheral nerves. *J Neurosci Methods* 123, 167–173, doi:10.1016/s0165-0270(02)00349-7 (2003).
58. Ollion, J., Cochenec, J., Loll, F., Escude, C. & Boudier, T. TANGO: a generic tool for high-throughput 3D image analysis for studying nuclear organization. *Bioinformatics* 29, 1840–1841, doi:10.1093/bioinformatics/btt276 (2013).

Figures

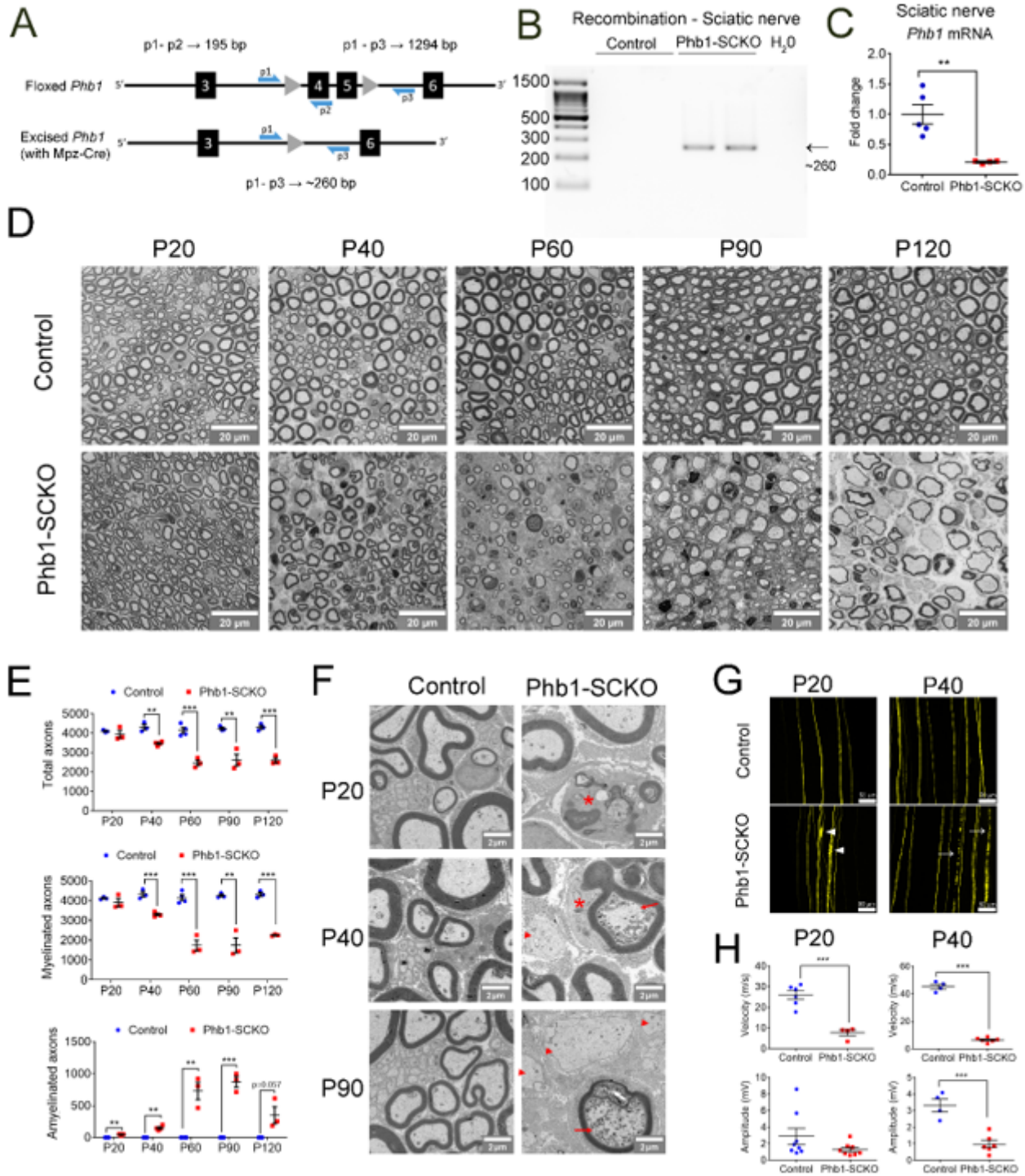


Figure 1

A progressive demyelination and axonal degeneration affect Phb1-SCKO animals. (a) Schematic representation of the floxed Phb1 allele. Exons 4 and 5 of the Phb1 gene are deleted upon Cre expression. Primers p1 and p2 were used for genotyping, while primers p1 and p3 were used to evaluate recombination. Square (exon), triangle (loxP site), half-arrow (primer). (b) Recombination PCR on DNA isolated from sciatic nerves reveals a ~260 bp recombined band in Phb1-SCKO animals, while unrecombined DNA is too long to generate an amplicon with our PCR conditions. (c) qRT-PCR analyses show a significant reduction in the level of Phb1 mRNA in nerve lysates of Phb1-SCKO mice. N=4-5 animals per genotype. Unpaired two-tailed t-test ($t=4.295$, $df=7$). (d) Representative images of cross sections of sciatic nerves. (e) The number of myelinated axons per sciatic nerve is greatly reduced in Phb1-SCKO animals starting at postnatal day 40 (P40) (middle). The decline can be explained both by demyelination (bottom) and axonal degeneration, evidenced by the reduction in the total number of axons (top). N=3-4 animals per genotype. Unpaired two-tailed t-test corrected for multiple comparisons using the Holm-Sidak method. Total axons [P20 ($t=0.816$, $df=4$), P40 ($t=6.508$, $df=5$), P60 ($t=8.08$, $df=5$), P90 ($t=5.257$, $df=4$), P120 ($t=10.608$, $df=4$)]; myelinated axons [P20 ($t=1.053$, $df=4$), P40 ($t=7.885$, $df=5$), P60 ($t=8.635$, $df=5$), P90 ($t=6.572$, $df=4$), P120 ($t=20.281$, $df=4$)]; amyelinated axons [P20 ($t=5.608$, $df=4$), P40 ($t=6.832$, $df=5$), P60 ($t=6.371$, $df=5$), P90 ($t=10.346$, $df=4$), P120 ($t=2.643$, $df=4$)] (f) Representative electron micrographs demonstrating the presence of degenerating axons (arrows), amyelinated/demyelinated axons (arrowheads) and Schwann cells degrading their own myelin (star) (g) Sparse labelling of axons in the tibial nerve using the Thy1-YFP reporter mouse indicates presence of axonal swelling at P20 (arrowheads) and axon fragmentation at P40 (arrows). N=3-4 animals per genotype. (h) A functional decline is detected in Phb1-SCKO animals by electrophysiological measurements, with a reduction in nerve conduction velocity as early as P20 and decreased amplitude of the CMAP starting at P40. N=4-8 animals per genotype. Unpaired two-tailed t-test. Velocity [P20 ($t=6.387$, $df=8$), P40 ($t=23.76$, $df=8$)]; Amplitude [P20 ($t=1.574$, $df=14$), P40 ($t=5.635$, $df=8$)]. * $p<0.05$, ** $p<0.01$, *** $p<0.001$.

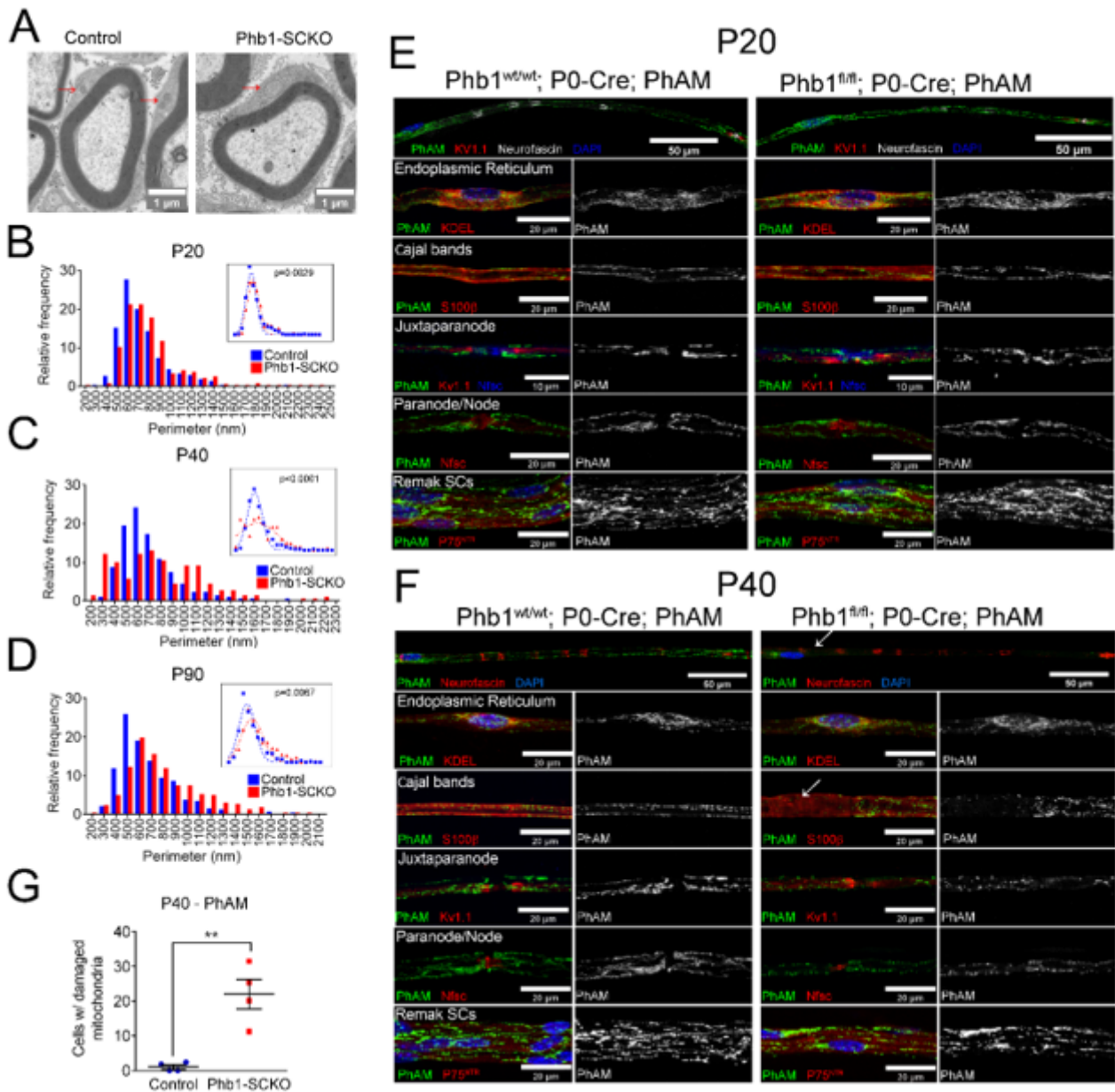


Figure 2

Ablation of Prohibitin 1 in Schwann cells results in altered mitochondrial morphology. (a) Representative electron micrographs highlighting the enlargement of mitochondria in sciatic nerves of Phb1-SCKO animals at P20 (arrows). (b-d) Mitochondria in SCs of PHB1-SCKO mice have a larger perimeter compared to mitochondria of control animals at P20 (b), P40 (c) and P90 (d). At P40, there is also a population of mitochondria that has a reduced perimeter, suggesting mitochondrial fragmentation. This population is lost at P90, suggesting that the fragmented mitochondria disappear. N=3 animals per genotype; at least 100 mitochondria from each animal were evaluated. Insets: Non-linear regression using a Gaussian curve followed by extra sum-of-squares F test [F(3,42) P20 = 5.482, F(3,38) P40 = 19.48, F(3,34) P90 = 4.813]. (e-f) Confocal z-projections of teased fibers of sciatic nerves of Phb1-SCKO mice and controls illustrating the morphology of Schwann cell mitochondria as labelled by the PhAM reporter. (e) At P20, there are changes in mitochondrial size. (f) At P40, some cells lack PhAM expression away

from the cell body. (g) PhAM is not detectable in about 20% of the myelin internodes of Phb1-SCKO animals at P40. N=4 animals per genotype. Unpaired two-tailed t-test ($t=4.866$, $df=6$).

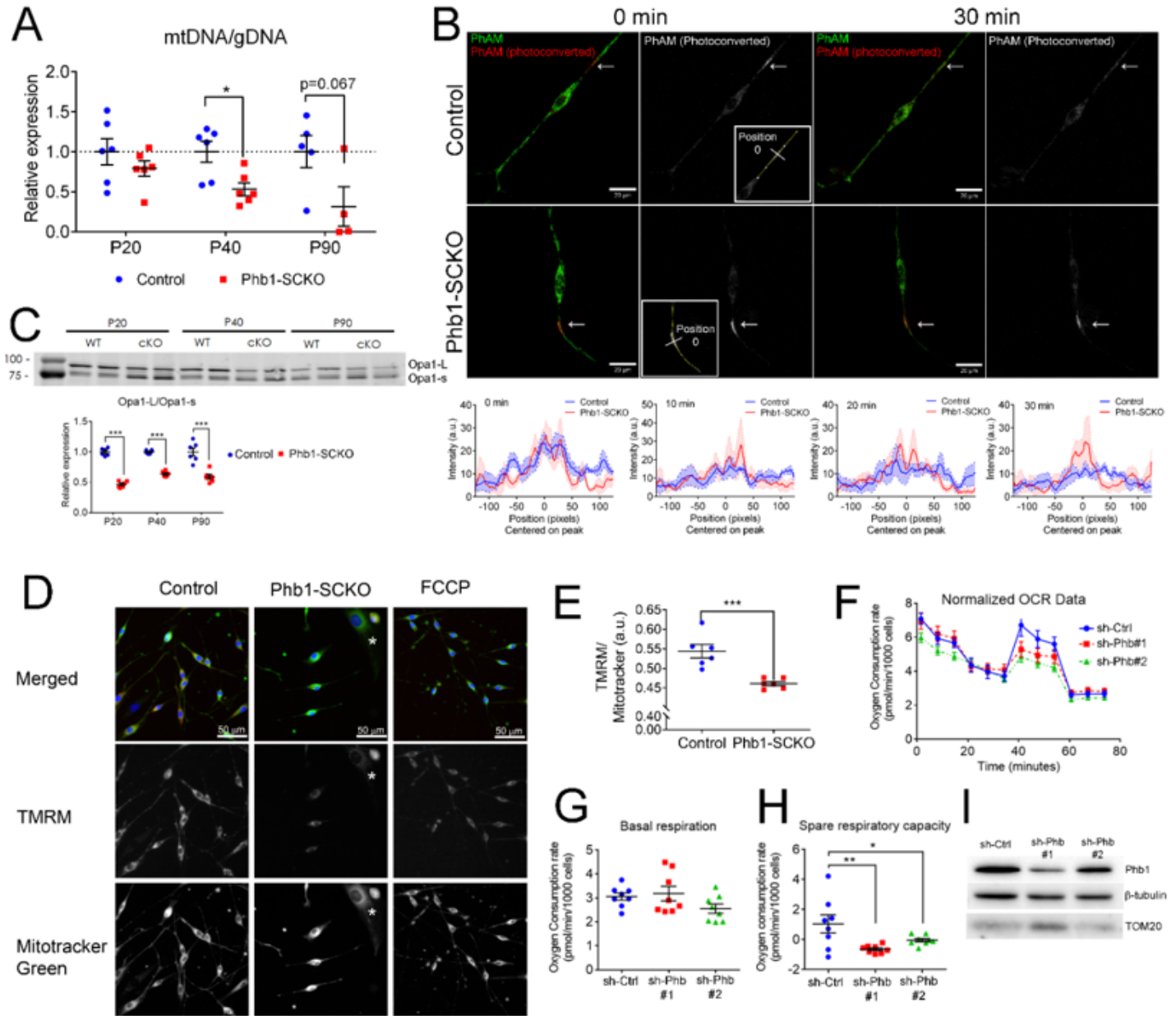


Figure 3

Mitochondria of Phb1-SCKO are dysfunctional. (a) The mitochondrial DNA (mtDNA) content is decreased in Phb1-SCKO mice starting at P40. N=4-6 animals per genotype. Unpaired two-tailed t-test corrected for multiple comparisons using the Holm-Sidak method [P20 ($t=1.114$, $df=10$), P40 ($t=3.068$, $df=10$), P90 ($t=2.174$, $df=7$)] (b) Mitochondrial dynamics is affected by deletion of Phb1 in primary mouse SCs. Top: PhAM fluorescence was photoconverted using a focal laser stimulation and dynamics of the photoconverted mitochondria (arrows) were observed for 30min. While the PhAM (photoconverted) signal quickly dissipated in the control SCs, it remained stagnant in Phb1-SCKO SCs. Inset: Position 0 represents the center of the stimulated area. Bottom: quantification of PhAM (photoconverted) signal around the stimulated area at different time points. Mean (line) and SEM (shaded area) of signal are reported. N=6-7

cells per genotype (c) Processing of the mitochondrial fusion protein Opa1 is increased in Phb1-SCKO mice. N=6 animals per genotype. Unpaired two-tailed t-test [P20 (t=16.664, df=10), P40 (t=17.015, df=10), P90 (t=5.335, df=10)] (d) Ablation of Phb1 leads to reduced mitochondrial membrane potential in primary SCs of PHB1-SCKO mice as compared to controls. N=6 wells per genotype. Unpaired two-tailed t-test (t=4.583, df=10). Asterisk: fibroblast. (e) Quantification of (d). (f-h) In primary rat Schwann cells, Seahorse analyses indicate that Phb1 knockdown does not change basal mitochondrial respiration (g), but impairs the spare respiratory capacity (h). (i) Western blot illustrating the reduction in levels of PHB1 upon treatment with shRNAs (63% and 21% reduction in PHB1/ α -tubulin ratio for sh-Phb #1 and sh-Phb #2, respectively). N=8 wells per condition. One-way ANOVA. F (2,21) = 5.594, p<0.05. * p<0.05, ** p<0.01, *** p<0.001.

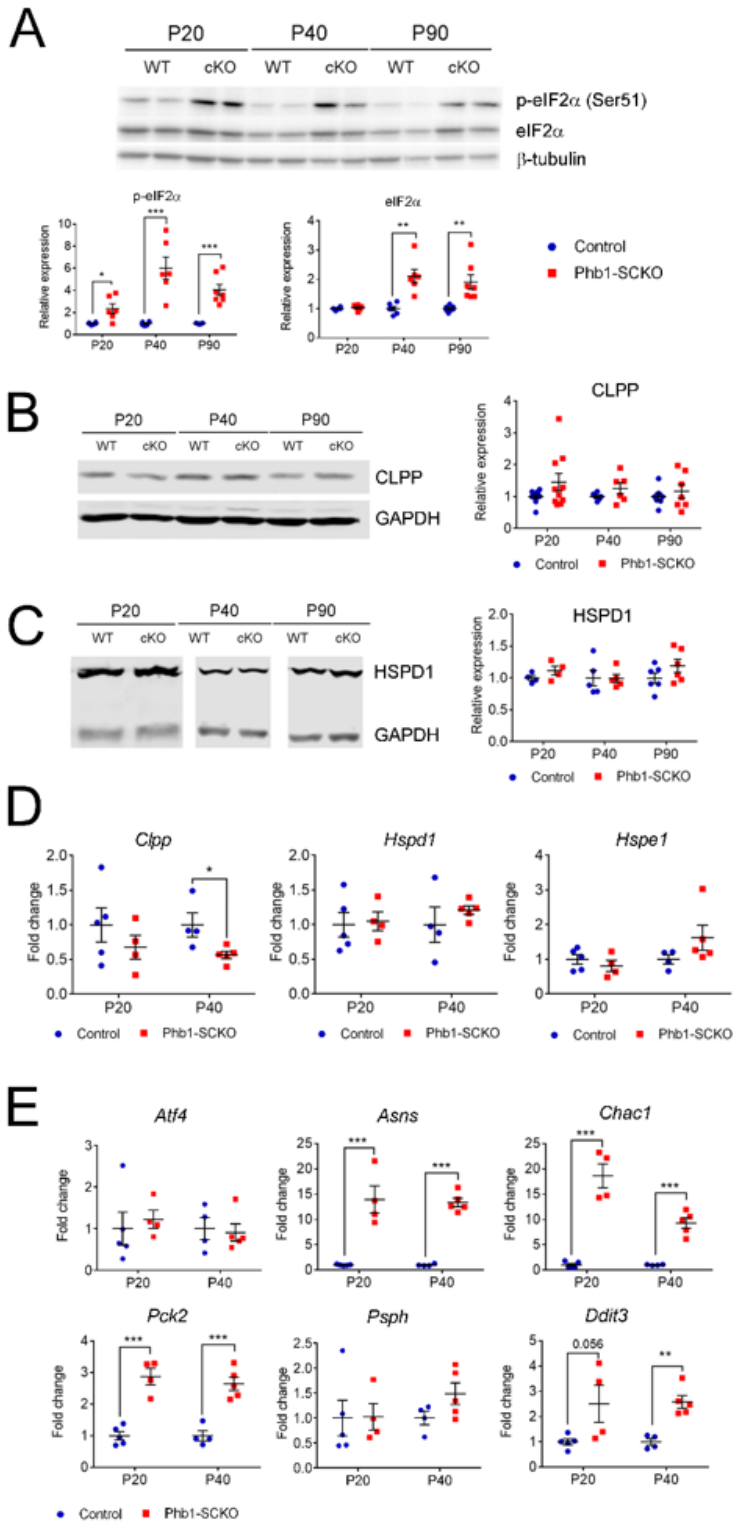


Figure 4

Deletion of Phb1 in SCs triggers a mitochondrial stress response. (a) p-eIF2 α is continuously upregulated in sciatic nerve lysates of PHB1-SCKO mice compared to controls, indicating activation of the ISR. N=6-7 animals per genotype. Unpaired two-tailed t-test. p-eIF2 α [P20 (t=3.068, df=10), P40 (t=4.948, df=10), P90 (t=6.088, df=12)]; eIF2 α [P20 (t=0.759, df=10), P40 (t=4.532, df=10), P90 (t=3.582, df=12)]. (b) Representative western blot for CLPP, a protease involved in the UPRmt response (left) and quantification

of relative expression levels at different time points (right). N=6-10 animals per genotype. Unpaired two-tailed t-test [P20 ($t=1.616$, $df=18$), P40 ($t=1.416$, $df=10$), P90 ($t=0.696$, $df=12$)]. (c) Representative immunoblot for HSPD1, a chaperone participating in the UPRmt cascade (left) and quantification of relative expression levels at different time points (right). N=4-5 animals per genotype. Unpaired two-tailed t-test [P20 ($t=1.46$, $df=6$), P40 ($t=0.057$, $df=8$), P90 ($t=1.46$, $df=10$)]. (d) qRT-PCR analysis of gene expression of Clpp, Hspd1 and Hspe1 (Hsp10). N=4-5 animals per genotype. Unpaired two-tailed t-test Clpp [P20 ($t=1.013$, $df=7$), P40 ($t=2.642$, $df=7$)]; Hspd1 [P20 ($t=0.217$, $df=7$), P40 ($t=0.9$, $df=7$)]; Hspd10 [P20 ($t=0.899$, $df=7$), P40 ($t=1.472$, $df=7$)]. (e) The mitochondrial stress response involves ATF4, as suggested by the upregulation of its targets. Asgn (asparagine synthetase), Chac1 (cation transport regulator-like protein 1), Pck2 (phosphoenolpyruvate carboxykinase 2), Ddit3 (DNA damage-inducible transcript 3), Psph (phosphoserine phosphatase). N=4-5 animals per genotype. Unpaired two-tailed t-test. Atf4 [P20 ($t=0.456$, $df=7$), P40 ($t=0.288$, $df=7$)]; Asns [P20 ($t=12.772$, $df=7$), P40 ($t=5.459$, $df=7$)]; Chac1 [P20 ($t=8.361$, $df=7$), P40 ($t=7.134$, $df=7$)]; Pck2 [P20 ($t=6.84$, $df=7$), P40 ($t=5.897$, $df=7$)]; Psph [P20 ($t=0.051$, $df=7$), P40 ($t=1.79$, $df=7$)]; Ddit3 [P20 ($t=2.292$, $df=7$), P40 ($t=5.113$, $df=7$)]. * $p<0.05$, ** $p<0.01$, *** $p<0.001$.

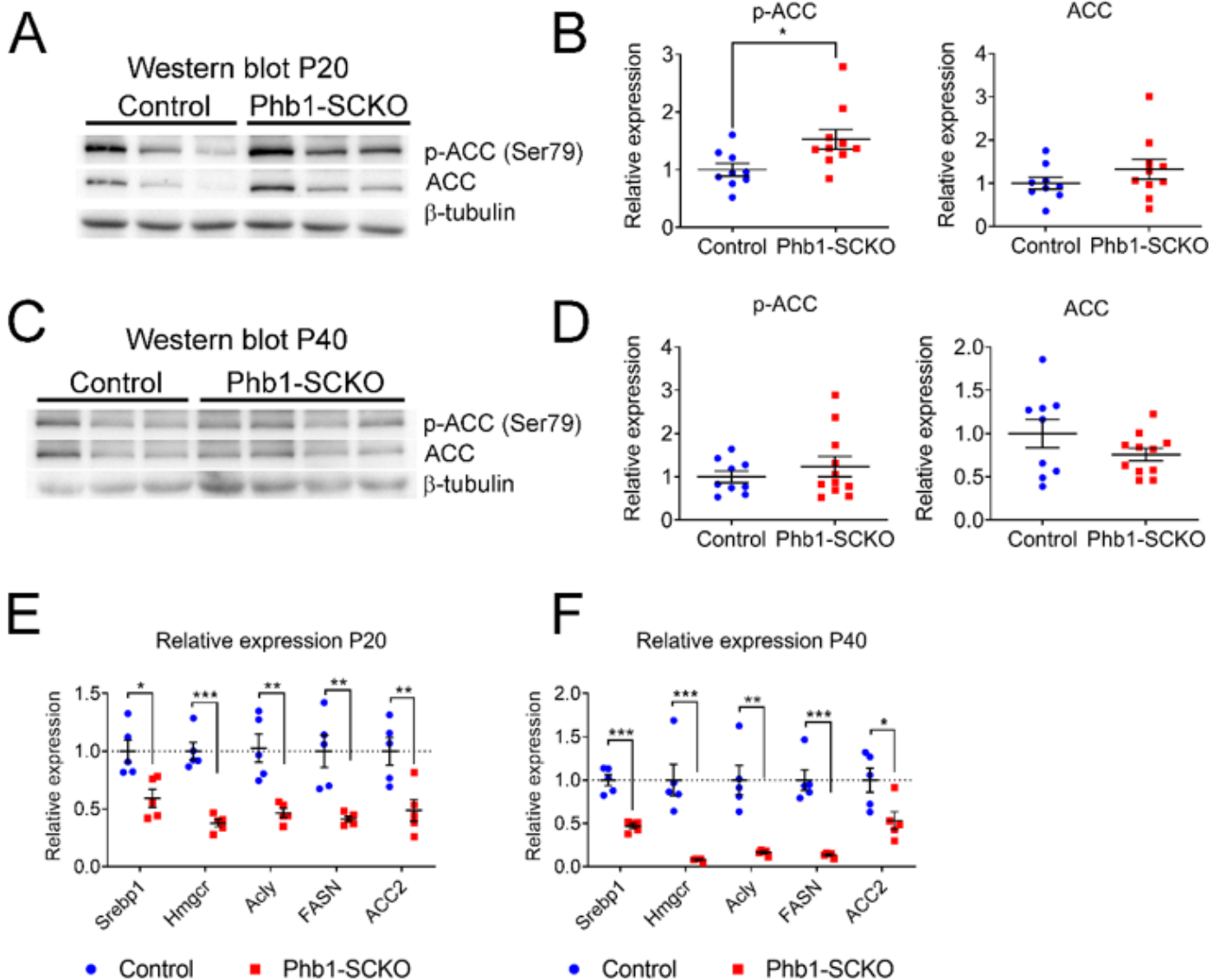


Figure 5

Deletion of Phb1 affects lipid metabolism. Western blot (a) and quantification (b) of ACC and p-ACC expression at P20. N = 6-7 animals per genotype. Unpaired two-tailed t-test [p-ACC ($t=0.4627$, $df=11$), ACC ($t=1.355$, $df=11$)]. Western blot (c) and quantification (d) of ACC and p-ACC expression at P40. N = 6-8 animals per genotype [p-ACC ($t=0.5447$, $df=12$), ACC ($t=1.153$, $df=12$)]. Unpaired two-tailed t-test. By qRT-PCR, we identified a significant downregulation of many enzymes involved with lipid biosynthesis at both P20 (e) and P40 (f). N = 5 animals per genotype. Unpaired two-tailed t-test P20 [Srebp1 ($t=3.26$, $df=8$), Hmgcr ($t=7.63$, $df=8$), Acly ($t=4.418$, $df=8$), FASN ($t=4.109$, $df=8$), ACC2 ($t=3.408$, $df=8$)]; P40 [Srebp1 ($t=7.551$, $df=8$), Hmgcr ($t=5.091$, $df=8$), Acly ($t=4.934$, $df=8$), FASN ($t=7.186$, $df=8$), ACC2 ($t=2.697$, $df=8$)]. * $p<0.05$; ** $p<0.01$; *** $p<0.001$.

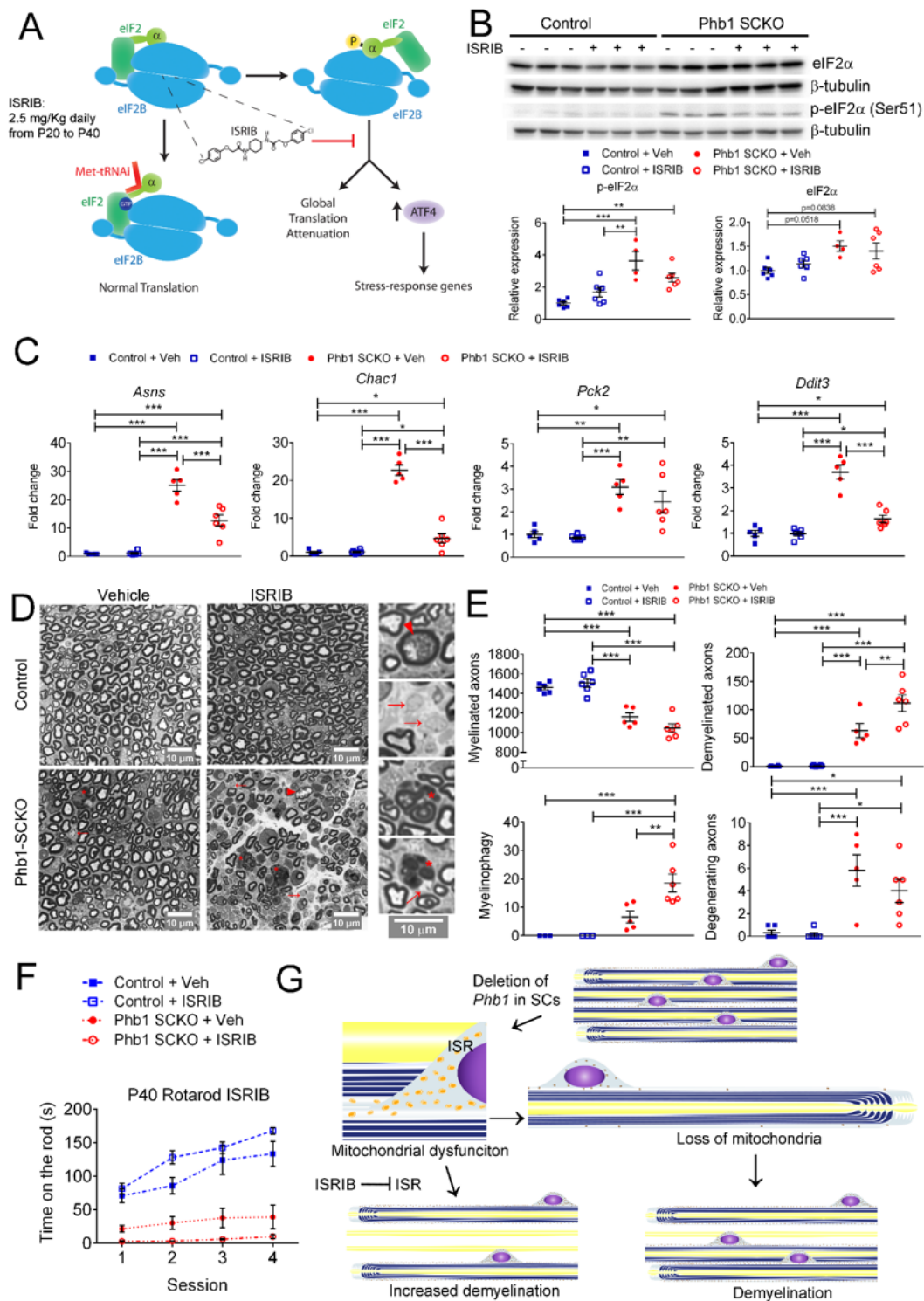


Figure 6

Induction of the ISR in Phb1-SCKO mice may be protective against demyelination. (a) Schematics of the mechanism of action of ISRIB. Animals received daily intraperitoneal injections of 2.5 mg/Kg ISRIB or vehicle (Veh) from P20 to P40 (b) ISRIB does not affect eIF2 α expression or phosphorylation (WB from sciatic nerve lysates). N=4-6 animals per group. Two-way ANOVA corrected for multiple comparisons using the Holm-Sidak method. eIF2 α : F (1,18) group = 11.29; p<0.01. p-eIF2 α F (1,18) group = 32.43,

$p < 0.001$; $F(1,18)$ interaction = 7.815; $p < 0.05$. (c) qRT-PCR analyses indicate that the expression levels of several ATF4 genes are reduced upon ISRIB treatment. $N=5-6$ animals per group. Two-way ANOVA corrected for multiple comparisons using the Holm-Sidak method. Asns: $F(1,18)$ group = 156.4, $p < 0.001$; $F(1,18)$ treatment = 18.3, $p < 0.001$; $F(1,18)$ interaction = 19.3, $p < 0.001$. Chac1: $F(1,18)$ group = 179.7, $p < 0.001$; $F(1,18)$ treatment = 90.61, $p < 0.001$; $F(1,18)$ interaction = 92.79, $p < 0.001$. Pck2: $F(1,18)$ group = 34.35, $p < 0.001$. Ddit3: $F(1,18)$ group = 84.51, $p < 0.001$; $F(1,18)$ treatment = 32.15, $p < 0.001$; $F(1,18)$ interaction = 31.04, $p < 0.001$. (d) Representative semithin images of tibial nerves. Inset show magnified images. Degenerating axon (arrowhead), demyelinated axons (arrows), myelin degradation (myelinophagy; stars). (e) ISRIB treatment leads to increased demyelination and myelinophagy in Phb1-SCKO mice. $N=5-6$ animals per group. Two-way ANOVA corrected for multiple comparisons using the Holm-Sidak method. Myelinated: $F(1,19)$ group = 98.01, $p < 0.001$. Demyelinated: $F(1,19)$ group = 85.58, $p < 0.001$; $F(1,19)$ treatment = 6.836, $p < 0.05$; $F(1,19)$ interaction = 6.469, $p < 0.05$. Myelinophagy: $F(1,19)$ group = 43.77, $p < 0.001$; $F(1,19)$ treatment = 9.938, $p < 0.01$; $F(1,19)$ interaction = 9.838, $p < 0.01$. Degenerating: $F(1,19)$ group = 32.17, $p < 0.001$. (f) Phb1-SCKO mice treated with ISRIB were the worst performing group in the rotarod test. Controls are significantly different from Phb1-SCKO mice (irrespectively of treatment; omitted for clarity). $N=5-6$ animals per group. Repeated measures two-way ANOVA corrected for multiple comparisons using the Holm-Sidak method. $F(3,19)$ group = 38.06, $p < 0.001$; $F(3,57)$ time = 37.24, $p < 0.001$; $F(9,57)$ interaction = 7.511, $p < 0.001$. (g) Schematic representation of the phenotype seen in Phb1-SCKO mice. * $p < 0.05$, ** $p < 0.01$, *** $p < 0.001$.

Supplementary Files

This is a list of supplementary files associated with this preprint. Click to download.

- [SupplementaryVideo1.mp4](#)
- [SupplementaryVideo2.avi](#)
- [SupplementaryVideo3.avi](#)
- [DellaFloraetal.SupplementaryInformation.docx](#)